Single-particle tracking localization microscopy reveals nonaxonemal dynamics of intraflagellar transport proteins at the base of mammalian primary cilia

T. Tony Yang[a], Minh Nguyet Thi Tran[a,†], Weng Man Chong[a], Chia-En Huang[a,‡], and Jung-Chi Liao[a,b,*]

[a]Institute of Atomic and Molecular Sciences, Academia Sinica, Taipei 10617, Taiwan; [b]Genome and Systems Biology Program, National Taiwan University, Taipei 10617, Taiwan

ABSTRACT **Primary cilia play a vital role in cellular sensing and signaling. An essential component of ciliogenesis is intraflagellar transport (IFT), which is involved in IFT protein recruitment, axonemal engagement of IFT protein complexes, and so on. The mechanistic understanding of these processes at the ciliary base was largely missing, because it is challenging to observe the motion of IFT proteins in this crowded region using conventional microscopy. Here, we report short-trajectory tracking of IFT proteins at the base of mammalian primary cilia by optimizing single-particle tracking photoactivated localization microscopy for IFT88-mEOS4b in live human retinal pigment epithelial cells. Intriguingly, we found that mobile IFT proteins "switched gears" multiple times from the distal appendages (DAPs) to the ciliary compartment (CC), moving slowly in the DAPs, relatively fast in the proximal transition zone (TZ), slowly again in the distal TZ, and then much faster in the CC. They could travel through the space between the DAPs and the axoneme without following DAP structures. We further revealed that BBS2 and IFT88 were highly populated at the distal TZ, a potential assembly site. Together, our live-cell single-particle tracking revealed region-dependent slowdown of IFT proteins at the ciliary base, shedding light on staged control of ciliary homeostasis.**

Monitoring Editor
Diane Lidke
University of New Mexico

Received: Oct 16, 2018
Revised: Jan 30, 2019
Accepted: Feb 4, 2019

INTRODUCTION

The primary cilium is an essential organelle responsible for multiple sensory and signaling activities (Goetz and Anderson, 2010). It originates from the mother centriole–derived basal body, with distal appendages (DAPs) at the periphery of the centriolar distal end anchoring the ciliary membrane at the ciliary base (Singla and Reiter, 2006; Ishikawa and Marshall, 2011; Tanos *et al.*, 2013). The protein complex of the transition zone (TZ) lies between the centriolar distal end and the ciliary compartment (CC), with a unique structure called Y-links bridging the axoneme and the ciliary membrane (Craige *et al.*, 2010; Hu *et al.*, 2010; Chih *et al.*, 2011; Garcia-Gonzalo *et al.*, 2011; Williams *et al.*, 2011). Proper functioning of the primary cilium relies on regulated ciliogenesis and receptor localization. Ciliogenesis is achieved by delivering precursors such as tubulins along the axoneme via intraflagellar transport (IFT), which is mediated by molecular motors and various IFT proteins (Kozminski *et al.*, 1993; Rosenbaum and Witman, 2002). Control of protein composition in cilia and flagella is achieved by gating in the TZ and DAPs (Reiter *et al.*, 2012; Tanos *et al.*, 2013).

To perform their functions, IFT proteins must migrate from the DAPs, the recruiting site of IFT proteins (Deane *et al.*, 2001), through the TZ, and into the CC. The TZ can serve as a screening site for protein entrance into the CC. Among all IFT proteins, IFT88 is one of the core molecules associated with the IFT-B subcomplex, which

This article was published online ahead of print in MBoC in Press (http://www.molbiolcell.org/cgi/doi/10.1091/mbc.E18-10-0654) on February 13, 2019.

Present addresses: †Institute of Biotechnology, Vietnam Academy of Science and Technology, Hanoi, Vietnam; ‡TFBS Bioscience, Inc., Taipei, Taiwan.

*Address correspondence to: Jung-Chi Liao (jcliao@iams.sinica.edu.tw).

Abbreviations used: 2D, two-dimensional; 3D, three-dimensional; BBS, Bardet–Biedl syndrome; CC, ciliary compartment; DAP, distal appendage; dSTORM, direct stochastic optical reconstruction microscopy; FBS, fetal bovine serum; GFP, green fluorescent protein; IFT, intraflagellar transport; MSD, mean square displacement; PBS, phosphate-buffered saline; SNR, signal-to-noise ratio; sptPALM, single-particle tracking photoactivated localization microscopy; TIRF, total internal reflection; TZ, transition zone.

is essential for molecular transport along the ciliary axoneme (Taschner *et al.*, 2012). Once ciliogenesis is initiated, IFT proteins assemble with molecular motors and adaptor proteins such as BBSome molecules, proteins of the Bardet–Biedl syndrome (BBS)-associated complex, which is important for cilium biogenesis, to facilitate precursor transport (Rosenbaum and Witman, 2002; Ou *et al.*, 2005). Although IFT proteins such as IFT52 are recruited to the DAPs, it is unclear whether this location is the site where the different IFT proteins assemble and where BBS proteins, molecular motors, and cargoes integrate with IFT proteins (Rosenbaum and Witman, 2002; Pedersen *et al.*, 2006; Wren *et al.*, 2013; Craft *et al.*, 2015). All of these proteins may be recruited to the DAPs and assembled there, or recruited there but assembled somewhere else, or individually recruited at different locations. One major missing link in the IFT process is how IFT proteins move between the DAPs and the ciliary axoneme. At the macromolecular scale, the ~130-nm distance between the tips of DAPs and the axoneme is relatively large. It is unclear whether DAP-recruited IFT proteins diffuse across the gap to the axoneme or whether they travel along the DAP structures.

Kymograph analysis has enabled particle tracking of anterograde and retrograde IFT dynamics along ciliary and flagellar axonemes (Snow *et al.*, 2004; Engel *et al.*, 2009; Wren *et al.*, 2013; Craft *et al.*, 2015). When it was integrated with total internal reflection (TIRF) microscopy and fluorescence recovery after photobleaching, signal-to-noise ratio (SNR) was much improved, and thus the mechanisms of IFT regulation along the cilia and flagella were further understood (Engel *et al.*, 2009; Wren *et al.*, 2013; Craft *et al.*, 2015). Kymograph studies have shown that IFT proteins move more slowly toward the base (Prevo *et al.*, 2015), but when examining the kymographs closely, one frequently sees an ultrabright "band" of IFT proteins present at the ciliary base (e.g., see Ye *et al.*, 2013), reflecting the ultrahigh density of IFT proteins packed in the tiny volume surrounding the DAPs and TZ at the ciliary base. Advanced imaging techniques have been implemented to track single molecules in flagella and cilia, including Fourier filtering to achieve single-molecule sensitivity for motors and IFT proteins (Prevo *et al.*, 2015; Mijalkovic *et al.*, 2017), low-concentration expression to track surface proteins SSTR3 and Smo (Ye *et al.*, 2013), and SNAP-tag labeling to track sporadic single-molecule events of Smo (Milenkovic *et al.*, 2015). However, none of these techniques addressed IFT protein dynamics at the highly dense area of the ciliary base.

Superresolution microscopy such as direct stochastic optical reconstruction microscopy (dSTORM) can be used to localize molecules at a high precision for fixed-cell imaging (Heilemann *et al.*, 2008). Single-particle tracking photoactivated localization microscopy (sptPALM) is a live-cell localization imaging technique for tracking a photoactivated subpopulation of fluorescent proteins, each emitting photons for a finite number of frames (Hess *et al.*, 2007; Manley *et al.*, 2008; Frost *et al.*, 2010; Hoze *et al.*, 2012; Rossier *et al.*, 2012; Izeddin *et al.*, 2014). It has been applied to study the dynamics of high-density molecules, including AMPA receptors, integrins, transcription factors, and actin assembly (Frost *et al.*, 2010; Hoze *et al.*, 2012; Rossier *et al.*, 2012; Izeddin *et al.*, 2014). Recently, sptPALM has been applied to reveal the dynamic interactions of IFT proteins in the ciliary compartment of *Caenorhabditis elegans* cilia (Oswald *et al.*, 2018). Diffusion analysis and distribution analysis of sptPALM data have been performed to reveal novel dynamic characteristics of biomolecules (Manley *et al.*, 2008; Meijering *et al.*, 2012; Persson *et al.*, 2013; Izeddin *et al.*, 2014). The challenge of using sptPALM to address specific biological problems is that every problem has unique characteristics such as molecular density, background noise, and speed of motion that require optimization of the sptPALM protocol.

Many important findings concerning IFT dynamics have been revealed by TIRF microscopy, which enables tracking of bright particles in flagella or cilia (e.g., see Engel *et al.*, 2009; Wren *et al.*, 2013; Craft *et al.*, 2015). sptPALM, on the other hand, is a single molecule–based assay, allowing short-distance tracking of single fluorophores when the particles are crowded or the fluorophores are normally hidden among other signals. For example, one may be able to observe motion of individual IFT proteins shown as the background fluorescence along the ciliary compartment, which is dimmer than that of moving IFT trains, or one may be able to see IFT dynamics in highly crowded regions such as the ciliary base and tip. Thus, sptPALM serves as a good complementary technique for TIRF microscopy for dynamic studies of IFT proteins.

In this study, we revealed novel IFT protein dynamics at the ciliary base by optimizing the sptPALM technique. With this unprecedented imaging capability for ciliary studies, we uncovered possible structural hindrance and preferred orientations along the paths IFT proteins travel, elucidating the mechanisms of different ciliogenesis-associated processes of IFT proteins, including protein assembly, microtubule track engagement, and passage gating.

RESULTS

sptPALM enabled dynamic studies of IFT proteins

We developed an sptPALM-based imaging protocol using photoconvertible fluorescent proteins to explore the dynamics of IFT proteins at the base of primary cilia. The excessive crowding of IFT proteins in this region and their high velocities necessitated multiparameter optimization of sptPALM to balance SNR, frame rate, trajectory duration, phototoxicity, and emission isolation. Human retinal pigment epithelial cells (hTERT-RPE-1; hereafter RPE-1) with stably expressed IFT88 fused to mEos4b, a monomeric photoconvertible protein (Paez-Segala *et al.*, 2015), were created. The cell morphology, average ciliary length, and ciliation frequency of this cell line were similar to those of wild-type RPE-1 cells. Single-molecule detection was achieved by implementing 405-nm photoconversion with its power being gradually and carefully incremented to photoconvert a finite population of IFT88-mEos4b fluorophores that could be optically isolated in this highly crowded region. These photoconverted fluorophores were then excited by a 561-nm laser (Figure 1A and Supplemental Movie S1). The laser power was optimized such that it had to be strong enough to reach an acceptable SNR while weak enough to extend the imaging duration to be as long as possible and weak enough to minimize phototoxicity. Similar to IFT88 in wild-type RPE-1 cells, IFT88-mEos4b also formed a high-intensity punctum at the ciliary base (Figure 1B). In contrast to most other sptPALM-based studies, which collect data from a cellular or subcellular volume of ~1000 μm^3, our imaging volume was usually confined to less than 1 μm^3, and thus the number of emitting events in each experimental run was very limited. Each of the photoconverted mEos4b emitting events was recorded as a short trajectory of IFT88 movement lasting several to tens of time points (Figure 1A). Imaging at 30 ms per frame was adopted to collect enough photons for single-molecule fitting while being fast enough to trace rapid diffusing movement of IFT88. Each experimental run lasted ~10,000 frames before significant photobleaching. Cilia with detectable twitching or shifting motion were excluded from the analysis to avoid any effect on IFT88 dynamics (Supplemental Figure S1). Simulated experimental runs were carried out to assure our displacement and velocity analyses were valid under the conditions of the sampling rate and the resolution of our experiments (Supplemental

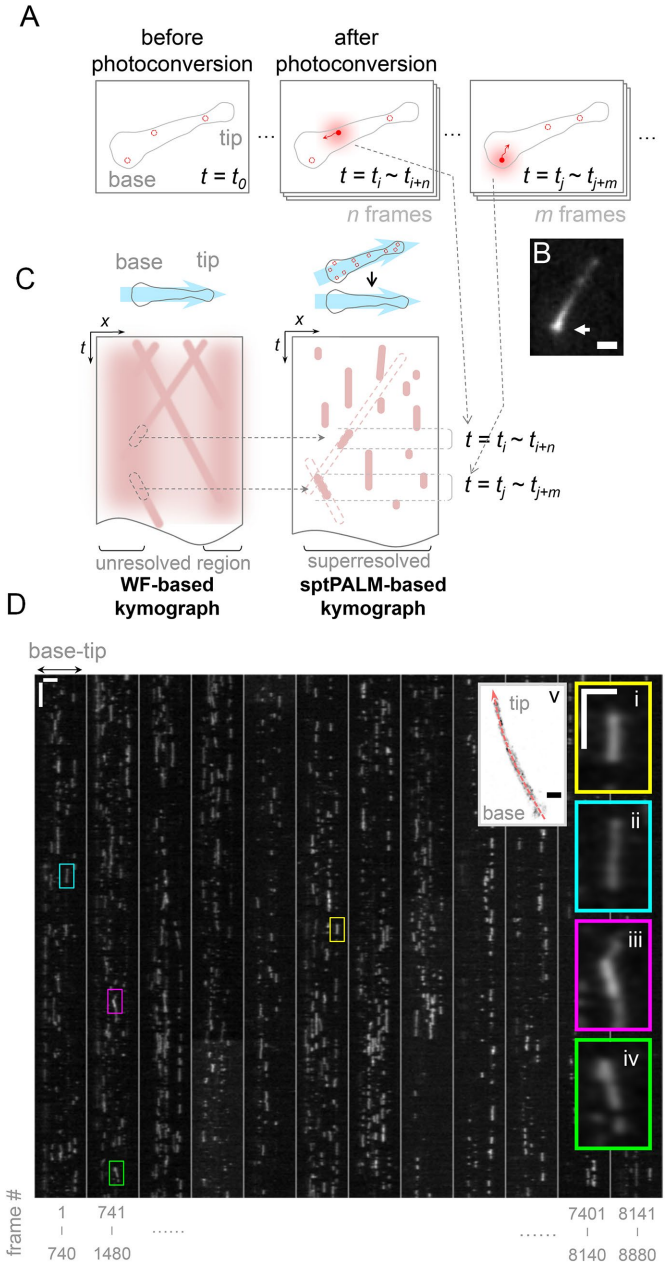

FIGURE 1: sptPALM-based imaging method for dynamic studies of IFT proteins in primary cilia. (A) Isolated single-particle tracking after photoconversion. Each probe stayed in the "on" state for several to tens of time points to create a short trajectory. (B) An epifluorescence image of IFT88-mEos4b showed a common bright punctum at the ciliary base (arrow), illustrating the high density of IFT proteins. (C) Each trajectory extracted from the defined curve along a primary cilium (blue arrow) was mapped to a trail in the kymograph (C, right); this is different from a wide-field (WF)-based kymograph, which usually cannot resolve individual molecules at the ciliary base (C, left). (D) A sectioned kymograph of thousands of IFT88-mEos4b trails was reconstructed and extracted from the line shown in the live-cell PALM image (panel v). One stationary and three moving IFT proteins (observed along the axoneme) are shown in panels i and ii–iv, respectively. Panel ii represents the retrograde motion, while the anterograde motion is shown in iii and iv. Scale bars: 1 μm (B); vertical, 1 s; horizontal, 2 μm (D, main panel); vertical, 500 ms; horizontal, 1 μm (D, i–iv) and 500 nm (D, v).

Figure S2). We have examined the effect of pH and found that, under the laser power we used (see *Materials and Methods*), our standard cell culture medium (pH 7.3–7.6) is close to optimal for the density and duration of the fluorophores at the base of primary cilia (Supplemental Figure S3).

Thousands of trails were observed in an experimental run, wherein each trail represented a short trajectory of IFT88-mEos4b. Compared with an ensemble-based assay, sptPALM enables isolation of events among the high density of IFT proteins packed in the tiny volume surrounding the DAPs and TZ (Figure 1C). Figure 1D and Supplemental Figure S4 show sectioned experimental kymographs reconstructed from single experimental runs for a living and a fixed cell, respectively. As representative examples, one stationary (or only moving laterally) molecule and three molecules moving longitudinally are shown in Figure 1D, i and ii–iv, respectively. The population of stationary IFT88 shown in Figure 1D, where many trails were vertical, was possibly the reason why background signals were observed in cilia or flagella (Engel *et al.*, 2009) and why single-particle tracking of IFT proteins at the base was so challenging.

To analyze dynamic characteristics of IFT88 molecules from the large number of localizations, we used an automated, computer-based algorithm to identify each single-particle position at each time point and to generate trajectories from these positions (see *Materials and Methods*). Even though the variations of kinematic properties may seem large in the ultimate conditional optimization of localization precision, the big data from such a large number of trajectories allow us to extract statistically meaningful information on IFT88 kinematics and dynamics.

The DAPs and the TZ accommodated not only axonemal but also transverse IFT88 movement

The recording of short localized trajectories for IFT88-mEos4b molecules enabled statistical analysis of their displacement directions at the ciliary base. All localizations of IFT88-mEos4b of one experimental run were overlaid as the outline of the cilium, with three trajectories showing possible paths of IFT88 at the ciliary base illustrated (Figure 2A and Supplemental Movies S2–S5). Despite dynamic transport of IFT88 proteins, the image with overlaid trajectories revealed the envelope of IFT88 axonemal distribution within the CC and the three-puncta organization at the ciliary base, agreeing with our previous findings (Yang *et al.*, 2013, 2015). One of these example trajectories showed an IFT88 molecule moving in the transverse direction from the periphery to the center of the ciliary base (Figure 2A and Supplemental Movie S3), illustrating the possibility of IFT protein movement not following the DAP or axonemal structures.

Other trajectories might not show clear direction of movement because of the combined effects of short durations and stochastic motion, as well as the noise-related uncertainty in localizing single molecules (Figure 2A and Supplemental Movies S4 and S5). Thus, to pinpoint the trajectories that represent directional movement, an effective displacement was defined by a simple linear regression fit of each trajectory of the mobile IFT proteins that spanned >45 nm (Supplemental Figure S5). Overlaid vectors of effective displacements from multiple primary cilia (straightening and alignment procedure shown in Supplemental Figure S6) showed surprising orientation differences between the cilium and the base. Most mobile IFT88 molecules within the CC moved approximately parallel to the longitudinal direction, while mobile IFT88 at the base, including the TZ and the DAPs, traveled at various angles (Figure 2, B and C, and Supplemental Figure S7). Within the DAPs and TZ, we observed

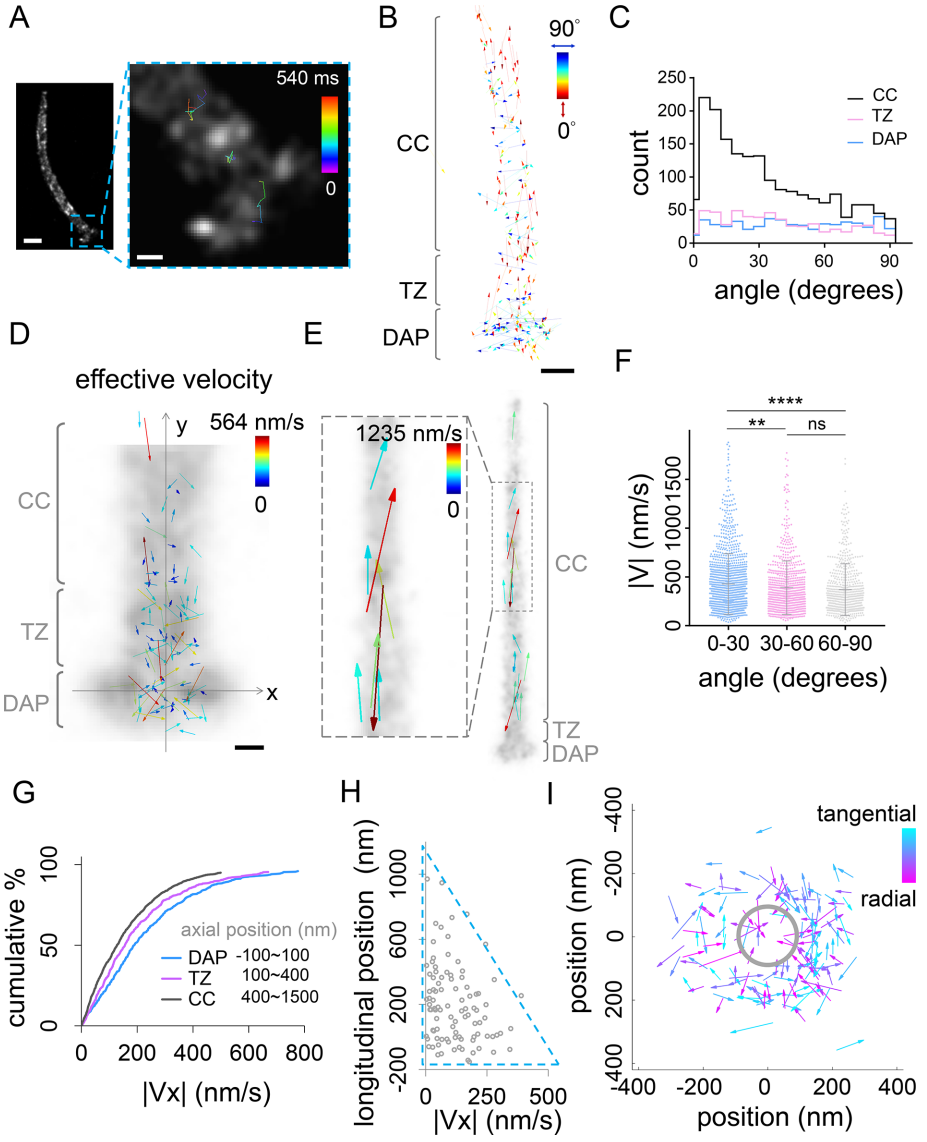

FIGURE 2: sptPALM trajectory analysis of IFT88 at the base of primary cilia showing distinct patterns of speed and direction of motion. (A) Live-cell localizations and three representative trajectories of IFT88-mEos4b. The overlaid image shows the envelope of the IFT88 axonemal distribution (left). Three trajectories of IFT88 at the ciliary base (right) show the paths of stationary and mobile IFT proteins. (B) Overlaid vectors representing effective displacements from one cilium revealed distinct angular distributions between cilium and base. The cilium (CC) had a large population of small-angle vectors, whereas the base exhibited a diverse angular distribution. (C) Detailed angular analysis from multiple primary cilia (2786 trajectories, 18 cilia) showed that the percentage of small-angle displacements (<30°) increased in the proximal–distal direction: DAPs < TZ < CC. The numbers of trajectories are 532, 563, and 1809 for DAP, TZ, and CC, respectively. (D) The effective velocity field calculated from the effective displacement and total travel time. (E) Representative fast-moving IFT proteins observed in the CC. (F) Statistical analysis of the orientation dependence of the effective velocity at the base were performed to compare three angular populations based on 2786 trajectories. The result suggests that high-speed IFT movement occurred when moving approximately parallel to the axoneme. The numbers of trajectories are 1333, 829, and 623 for 0–30, 30–60, and 60–90 degrees, respectively. Statistics notation: ****, $p < 0.0001$; **, $p < 0.01$; ns, not significant. (G) Cumulative population plot of lateral speed (V_x) shows that it was higher in the DAP and TZ regions than in the CC. The numbers of trajectories are 517, 545, and 1713 for DAP, TZ, and CC, respectively. (H) The upper bound of the V_x distribution decreased with longitudinal position. (I) Axial view of sptPALM-based analysis revealed that IFT88 proteins of nonciliated cells could travel radially between the DAPs and axoneme as well as moving tangentially. Scale bars: 500 nm (A); 100 nm (A, enlarged panel, D); 200 nm (B).

many translocations at nearly 90°, suggesting that IFT proteins might travel transversely with their nonaxonemal degrees of freedom in the space. Flux analysis of the IFT88 trajectories showed that our system approximately reached a steady state (Supplemental Figure S8).

IFT proteins had a lower transverse velocity toward the ciliary compartment

The effective velocity calculated from the effective displacement indicated that some IFT proteins moved faster than others in a location- and orientation-dependent manner (Figure 2D). Fast-traveling IFT proteins in the CC had a mean effective velocity of ~600 nm/s (Figure 2E), consistent with the velocity reported in the literature (Tran *et al.*, 2008; Besschetnova *et al.*, 2010), confirming that our assay did not perturb IFT dynamics. Note that imaging of this work based on two-dimensional (2D) projection of three-dimensional (3D) data might potentially hide a certain fraction of information of the motion in the *z* direction. This may cause an underestimation of transport rate of molecules by a factor of $\sim\sqrt{2}/\sqrt{3}$ on average for an axially symmetric distribution of movement, because only the speed as projected onto a 2D plane was measured. However, because of the approximately cylindrical symmetry of a cilium, it is unlikely that a large proportion of molecules traveling orthogonal to the imaging plane. Therefore, although the quantitative measurements may not be precise, the qualitative conclusions of results here and following were not affected by the 2D projection of 3D data. Analyzing the orientation dependence of the effective velocity at the base, we found that high-speed IFT movement (e.g., $V > 500$ nm/s) occurred statistically more frequently when motion was approximately parallel to the longitudinal axis of the cilium (0/30°; Figure 2F), possibly suggesting that axoneme-associated translocation exhibited high speed, but it happened only occasionally. The fast-moving IFT88 at the base was slower than its fast-moving equivalents in the CC, and this may be due to the more crowded and intricate architectures of the DAP and TZ hindering movement.

To investigate the dependence of transverse velocity on longitudinal position, we extracted the lateral component of velocity (V_x) for each moving trajectory. Consistent with our findings regarding displacement, IFT88 exhibited higher lateral speed in the DAP and TZ regions than in the CC (Figure 2G). Interestingly, IFT proteins still

possessed a considerable lateral speed at the TZ, suggesting that the space close to the Y-links allows lateral movement (Figure 2H). Overall, our sptPALM-based study revealed distinct patterns for IFT88 transport along primary cilia, implying different molecular hindrances due to varying molecular architectures or population densities need to be tested at different locations.

A localized axial view revealed radial transport of IFT proteins at the DAPs

Although the lateral view showed the transverse movement of IFT proteins at the DAP region, it was unclear whether these proteins traveled along the periphery of the DAPs or radially between the DAPs and the axoneme/centriole. An axial view of IFT88 movement (here molecules were observed in nonciliated centrioles) revealed that some IFT proteins moved tangentially to the periphery, while others moved radially. Therefore, IFT proteins could indeed travel between the DAPs and the axoneme through the space in between (Figure 2I), and the directions of travel spanned all angles, suggesting that the movement was not guided by the pinwheel-like DAP blades. We also used fixed-cell superresolution microscopy to show that the distribution patterns of IFT88 close to the DAPs were similar for both ciliated and nonciliated centrioles (Supplemental Figure S9), suggesting IFT88 traveled in random orientations in this region regardless of whether the cilium formed or not. This observation is consistent with our previous finding that the DAP matrix is where IFT88 proteins settle (Yang *et al.*, 2018), implying the matrix is a region that allows dynamic movement of proteins within.

Diffusion analysis and consecutive displacement analysis indicated that IFT protein movement was more diffusive at the proximal TZ than at the distal TZ

To further refine the spatial resolution of our dynamic characterization, we performed frame-by-frame consecutive displacement analysis for each trajectory. The map of the displacement of every two consecutive points from a trajectory showed location-dependent displacement of IFT proteins (Figure 3A). A relatively large fraction of large displacements were detected at the proximal region of the TZ (Figure 3B), suggesting that the proximal TZ may support a fast-moving environment for IFT proteins, significantly different from the distal TZ region, where smaller translocation steps were observed (Figure 3C).

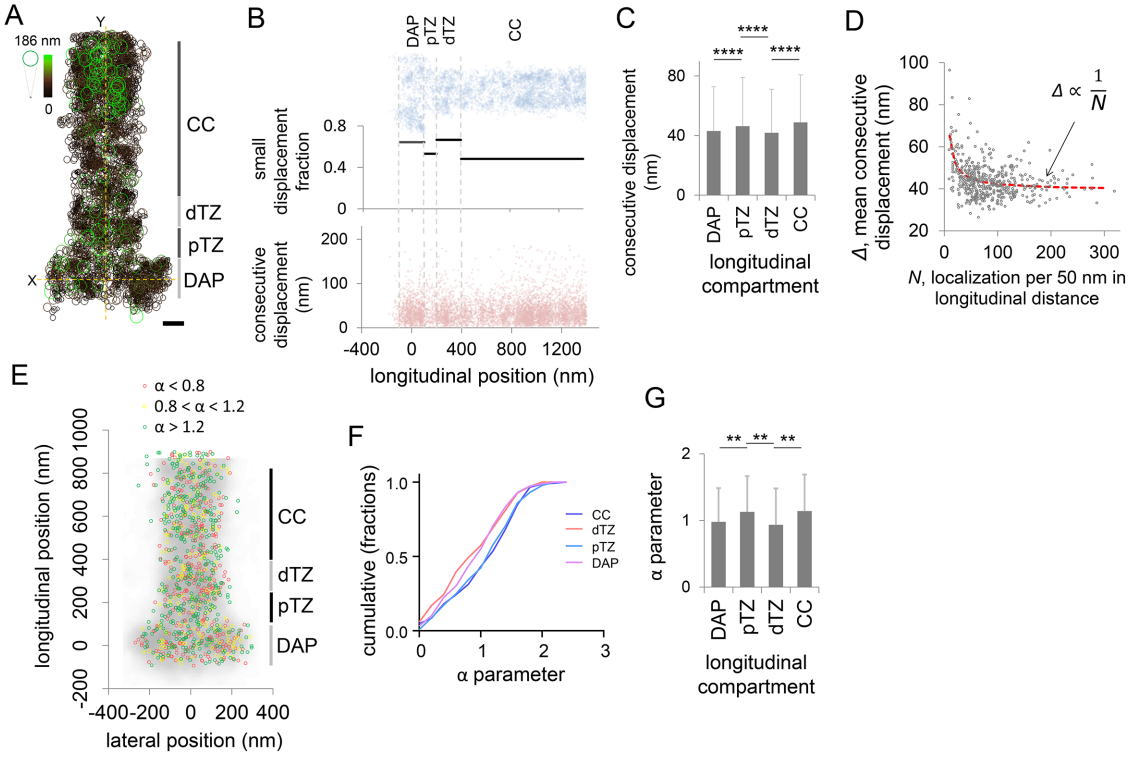

FIGURE 3: Consecutive displacement and diffusion analyses showing longitudinal dependence of IFT protein dynamics. (A) Consecutive displacement map of IFT88 from data of three cilia displayed differential characteristics of movement between the proximal TZ (pTZ) and the distal TZ (dTZ). (B) Localization map (blue) and consecutive displacements (pink) from data in A, revealing that small consecutive displacement (<45 nm) was relatively populated at the DAP and the dTZ (middle). The numbers of steps calculated are 1085, 235, 637, and 3619 for the DAP, pTZ, dTZ, and CC, respectively. (C) Statistics of consecutive displacement calculated from ~18,000 translocation steps of ~2800 trajectories in 18 cilia showing different translocation step sizes of the DAP, pTZ, dTZ, and CC. The numbers of steps calculated are 7185, 4003, 3675, and 3618 for the DAP, pTZ, dTZ, and CC, respectively. (D) Relationship between mean local displacement and localization density illustrating that the high population regions accommodate slow-moving molecules. Solid line represents the fitting result. (E) Classification of each trajectory based on diffusion characteristics (α) was mapped onto an averaged superresolved image of a primary cilium to show its location dependence. (F) Cumulative probability distribution plot of α value from the data based on 15 cilia (663 trajectories) and (G) statistical analysis of longitudinal position dependence showed that IFT protein trafficking was less diffusive at the dTZ and DAP but more diffusive at the pTZ and CC. The numbers of trajectories are 255, 128, 136, and 144 for the DAP, pTZ, dTZ, and CC, respectively. Scale bar: 100 nm (A). Statistics notation: ****, $p < 0.0001$; **, $p < 0.01$, Student's *t* test. Error bars represent SD.

The distal TZ, which is close to the location of the Y-links, might contain molecules hindering the motion of IFT proteins. Relatively small displacement was also observed at the DAP region (Figure 3, B and C). Analyzing location-dependent consecutive displacements, we found that regions with a higher IFT88 population density accommodated molecules that have a smaller mean consecutive displacement, and vice versa (Figure 3D), supporting the hypothesis of obstructing movement at the distal TZ and the DAP region.

Diffusion analysis based on mean square displacement (MSD; see *Materials and Methods*) further supports our observation in consecutive displacement analysis, revealing distinct diffusion mechanisms at the ciliary base (Figure 3, E and F). We found that IFT proteins moved more directionally in the CC, whereas diffusion modes were considerably more heterogeneous in the TZ and DAPs. Statistical analysis of the dependence of the diffusive parameter α on longitudinal position showed that IFT protein movement was less diffusive at the distal TZ than in the neighboring regions (Figure 3G).

Combining the comparison of consecutive displacement and diffusion parameter, we thus concluded that IFT88 molecules change dynamic characteristics multiple times along the ciliary path, moving slowly in the DAP region, relatively fast in the proximal TZ, slowly again in the distal TZ, and then much faster in the CC.

Two-color superresolution imaging revealed that the distal TZ is a potential assembly site

To understand why DAPs, proximal TZ, and distal TZ had different IFT88 dynamic characteristics, we examined where IFT88 might interact with other proteins, specifically KIF3A, the kinesin responsible for anterograde movement carrying IFT proteins in the CC, and BBS2, one of the BBSome components serving as an adaptor between IFT88 and cargo proteins (Nachury *et al.*, 2007), in fixed RPE-1 cells. Two-color dSTORM superresolution imaging of BBS2 and IFT88 revealed that BBS2 molecules were highly populated in the CC and distal TZ, but they were considerably sparse in the proximal TZ and absent in the DAPs (Figure 4A). An image overlaying

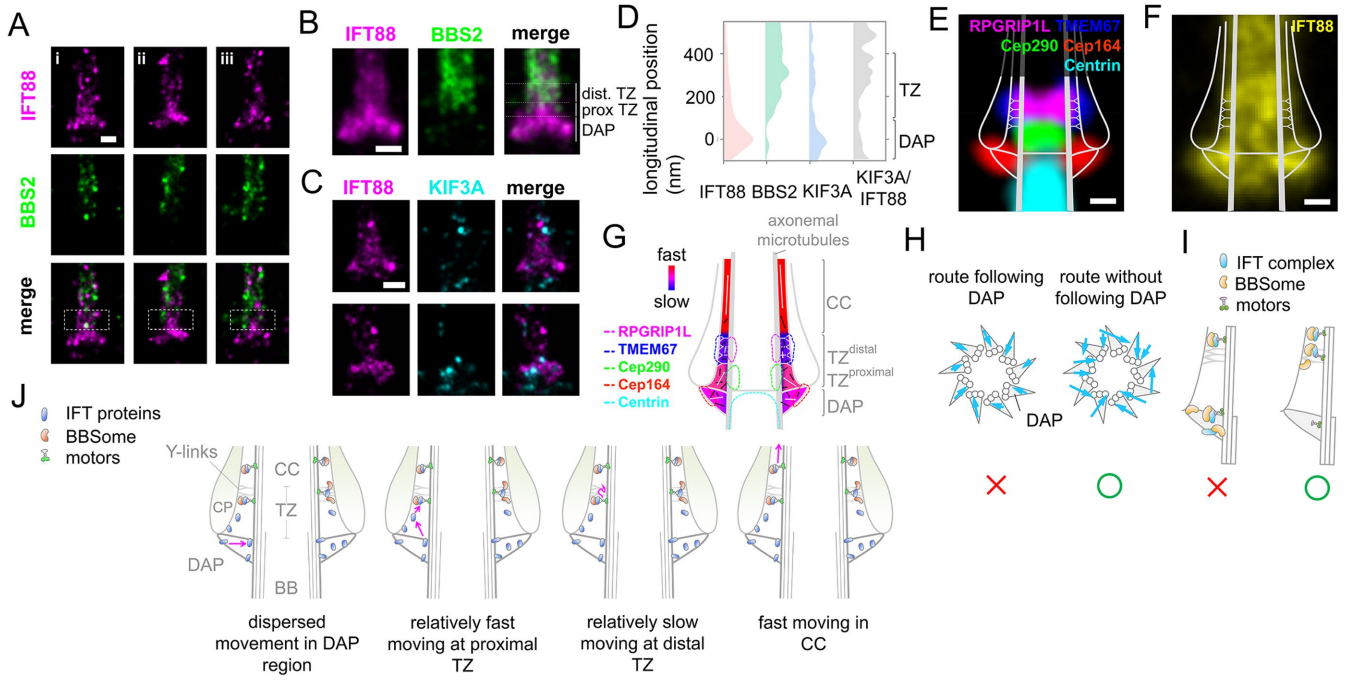

FIGURE 4: Superresolution imaging studies supporting a model of IFT protein trafficking in different regions of the ciliary base. (A) Two-color superresolution images of BBS2 and IFT88 showing that BBS2 molecules were nearly absent at the DAPs and sparsely localized at the TZ (white box), more toward the distal end. (B) Overlaid superresolution images of multiple cilia ($n = 11$) illustrate that BBS2 and IFT88 primarily overlapped at the distal TZ. (C) Two-color superresolution images of KIF3A and IFT88 revealing that, unlike IFT88, KIF3A is less populated at the ciliary base. (D) Comparison of population distributions of IFT88, BBS2, and KIF3A quantitatively suggests their spatial coincidence for potential interactions. The ratio of KIF3A/IFT88 implies the relative probability for each IFT88 molecule to find a KIF3A molecular motor. $n = 11$ cilia for IFT88 and BBS2; $n = 13$ for KIF3A. (E) Superresolution molecular mapping of TZ/DAP proteins (RPGRIP1L, TMEM67, Cep290, Cep164, and centrin) indicated TZ proteins assembled into distinct layers; for example, RPGRIP1L and TMEM67 at the distal TZ and Cep290 at the proximal TZ (Yang *et al.*, 2015). The distal TZ is close to the longitudinal location of the Y-links. (F) IFT88 proteins were highly populated at the DAPs and distal TZ. (G) Map summarizing the sptPALM results in terms of IFT protein speed and direction. Movement of IFT proteins was slow near the distal TZ and fast in the proximal TZ. (H) Our results enable discrimination of different hypotheses. IFT88 traveling from the recruiting site to the axoneme does not follow the "blades" of DAPs but instead moves in random directions when observed in an axial view. (I) The assembly of IFT88 and BBS2 will most likely occur at the distal TZ region. It is nearly impossible for this assembly to happen at the DAPs, because BBS2 is absent there. (J) Model illustrates the movement of an IFT protein at different regions from the DAPs to the CC: 1) dispersed and relatively slow movement in the DAP region, including inward movement from the tip of the DAPs to the axoneme; 2) relatively fast motion in the proximal TZ with a trajectory that can reach the space enveloped by the ciliary pocket; 3) slow motion at the distal TZ close to the Y-links, where assembly with molecules such as BBSome proteins may occur; and 4) engagement onto the microtubule track to facilitate fast movement along the axis of the CC. Scale bars: 200 nm (A–C); 100 nm (E, F).

data from multiple cilia clearly illustrates differential localization of IFT88 and BBS2, with overlapping region of these two proteins primarily at the distal TZ, and some in the CC (Figure 4B). That is, the distal TZ, or possibly the CC, could serve as an assembly site for IFT88 and BBS2. This result might explain why we saw the slowest motion of IFT88 in the distal TZ.

Two-color superresolution images of KIF3A and IFT88 showed that, although we could see KIF3A molecules distributed along the cilia as expected, the population of KIF3A was considerably sparse in the region where IFT88 molecules were highly populated (Figure 4C). That is, only a finite number of molecular motors were available to carry IFT88 molecules into the CC. Population analysis of IFT88, BBS2, and KIF3A along the longitudinal axis shows relative populations that might reflect the assembly probability in different locations (Figure 4D). As KIF3A was less populated in the ciliary base than IFT88, KIF3A should be the limiting factor for their assembly. The ratio of KIF3A/IFT88 implies that the relative probability for each IFT88 molecule to find a KIF3A molecular motor was higher toward the distal TZ.

DISCUSSION

Ciliogenesis requires IFT within the CC, and this in turn requires IFT protein recruitment to the ciliary base, followed by IFT complex assembly, IFT protein–motor assembly, track engagement onto the axoneme, integration with cargoes, and ciliary entrance screening. All these processes occur at the ciliary base, where ensemble-based images show a highly crowded population of IFT proteins, whose individual trajectories of motion are impossible to delineate by conventional microscopy. This makes elucidation of these processes very challenging. By tracking stochastically photoconvertible molecules that can be isolated from one another for a short time, we demonstrated that sptPALM largely meets the needs of studying IFT protein dynamics at the ciliary base. Although individual mEos4b-IFT88 trajectories were relatively short, analysis of the aggregated trace data was sufficient to reveal the characteristics of spatiotemporal dynamics of IFT proteins at the base of mammalian primary cilia.

To better understand our results on the ciliary structural framework, we mapped the localizations onto the superresolved molecular architecture of the TZ and DAPs to find location-dependent dynamic characteristics of IFT proteins on the ciliary structural framework (Figure 4, E–G; Yang *et al.*, 2015). Mobile IFT88 proteins travel slowly at the DAP region, fast at the Cep290-neighboring proximal TZ, very slowly through the distal TZ close to the Y-links, and very fast in the CC (Figure 4G).

Mobile IFT88 proteins traveled between DAPs and the axoneme according to varied patterns, moving in different directions with a relative slower speed when compared with IFT88 proteins in other regions. This means some areas between the DAP tips and the centriolar axoneme can accommodate IFT88 movement in constrained dynamic characteristics, potentially suggesting that some areas in the DAP region may allow IFT88 movement in an obstructive environment. The obstruction may come from the pinwheel-like structure of the DAPs or some other densely distributed molecules not apparent in the electron micrographs. This finding is not only consistent with our finding that the DAP matrix acts as the transmembrane protein gate (Yang *et al.*, 2018), potentially pausing IFT88 movement through screening, but also agrees with the finding of a second periciliary diffusion barrier of membrane proteins at this level (Ye *et al.*, 2018).

IFT88 in the proximal TZ, where Cep290 is localized, exhibited dynamics that were considerably different from those in adjacent regions. As IFT proteins entered the proximal TZ, they moved faster relative to the adjacent DAP and distal TZ regions in a less constrained manner. They were also less concentrated in this region than in the DAP region and the distal TZ. We hypothesize that the proximal TZ has fewer obstructive structures or it is not an assembly site for protein complexes, so IFT proteins do not get held up in this region. This is the location Ye *et al.* (2018) proposed as the intermediate compartment. Widely distributed IFT88 proteins, filling the space between the axoneme and the ciliary pocket, show that they are not necessarily engaged onto microtubule tracks at the proximal TZ, suggesting that a proportion of the IFT proteins in this region may not integrate with motor proteins.

The distal TZ is another region where mobile IFT proteins slow down. This is the area where several TZ proteins such as TMEM67, TCTN2, MKS1, and RPGRIP1L are found and Y-links are located (Yang *et al.*, 2015), suggesting that IFT proteins may dwell in the region close to the Y-links. That is, this region constrains their motion to a greater degree, possibly owing to the structural hindrance provided by Y-links. That IFT proteins are held up in this area suggests that some functional activities may occur here, possibly assembly of IFT proteins with other molecules, such as molecular motors or cargoes, or entrance screening performed by Y-link proteins (Reiter *et al.*, 2012). Several dynamic studies have found the TZ to be the diffusion barrier (Nachury *et al.*, 2010; Chih *et al.*, 2011; Kee *et al.*, 2012; Ye *et al.*, 2013, 2018; Oswald *et al.*, 2018), and our study further confines the region to the distal TZ. Once IFT proteins pass through the TZ and enter the CC, their motion becomes faster and more unidirectional, suggesting full integration with molecular motors engaged onto the microtubule tracks. Our angular distribution analysis for each region shows that more and more IFT proteins move in the longitudinal direction as one goes from the DAPs to the TZ to the CC, suggesting that motor assembly and axonemal engagement increases in the proximal–distal direction.

Our studies allow us to reject some hypotheses and find support for others. One surprising finding is that IFT88 traveling from the recruiting site to the axoneme does not follow the "blades" of DAPs (Figure 4H). Instead, IFT88 molecules move in random directions when observed in axial view, potentially migrating with the DAP matrix region (Yang *et al.*, 2018). Another finding is that IFT88 molecules can wander in the space enveloped by the DAPs, the axoneme, the ciliary membrane, and the Y-links. Unexpectedly, they are not entirely axoneme bound or membrane bound when traveling in the proximal TZ region, but are moving stochastically within this volume. Finally, for complex assembly, it has been shown that various BBS proteins, including BBS2, travel processively in the CC (Wei *et al.*, 2012). We found that the assembly of IFT88 and BBS2 most likely occurs at the distal TZ region (Figure 4I). It is nearly impossible for this assembly to happen at the DAPs, because BBS2 is absent there. Based on the results presented here, we propose a model summarizing different dynamic characteristics of IFT88 at the DAPs, the proximal TZ, the distal TZ, and the CC (Figure 4J).

MATERIALS AND METHODS

Cell lines and culture

Human retinal pigment epithelial cells (hTERT-RPE-1) were cultured in DMEM/F-12 (11330-032; Thermo Fisher Scientific [Life Technologies], Waltham, MA) supplemented with 10% fetal bovine serum (FBS) (10437-028; Thermo Fisher Scientific) and 1% penicillin–streptomycin (15140-122; Thermo Fisher Scientific [Life Technologies]). HEK293T cells were cultured with DMEM (11965-084; Thermo Fisher Scientific [Life Technologies]) with 10% FBS and 1% penicillin–streptomycin. All cells were cultured at 37°C under 5% CO_2.

Cloning and lentivirus generation

IFT88-mEos4b plasmids were generated by replacing the green fluorescent protein (GFP) sequence in the pLVX-tight puro human IFT88-GFP plasmid (Tet-On), a gift from W. J. Wang (National Yang Ming University, Taipei, Taiwan), with the mEos4b sequences from the pRSETa_mEos4b plasmid (51073; Addgene, Cambridge, MA). Briefly, the insert (mEos4b) was amplified with a forward primer containing an *Mlu*I restriction site and a reverse primer containing a *Bsr*GI restriction site. The primer sequences were 5′-ACGCGTGCCACCATGGTGAGTGCGATT-3′ (forward) and 5′-GCCTGTACATTATCGTCTGGCATTGTCAGG-3′ (reverse). Both the insert and the vector (IFT88-GFP) were digested with *Mlu*I (R0198; New England Biolabs, Ipswich, MA) and *Bsr*GI (R0575; New England Biolabs) before ligation. The ligated product was transfected into DH5α-competent cells (RH617; RBCBioscience, Chungho, Taipei, Taiwan) to obtain the desired clone. The plasmid sequence was confirmed using DNA sequencing. An IFT88-mEos4b lentivirus was generated by cotransfection of the IFT88-mEos4b plasmid with packaging and envelope vectors (PT-5144-1; Clontech, Mountain View, CA) into HEK293T cells using a TransIT-293 Transfection Reagent Kit (MIR 2700; Mirus, Madison, WI). The cell culture medium containing the virus was collected 3 and 4 d after transfection. The medium was centrifuged and filtered to remove cell debris. The virus was kept at −80°C until later use.

Stable clone generation and sample preparation

For generation of RPE-1 cells stably expressing IFT88-mEos4b, cells were infected with the IFT88-mEos4b lentivirus and then selected with 5 µg/ml puromycin (p8833; Sigma-Aldrich, St. Louis, MO) for 2 wk to obtain a stable cell pool. Medium was refreshed every 3 d. For creation of a single clone, the cell pool was distributed into the wells of a 96-well plate at a density of 1 cell per well and selected with puromycin for 2 wk. For preparation of a sample for localization study, cells were seeded onto poly-L-lysine (P1274; Sigma-Aldrich)-coated coverslips, and were starved for 2 d before fixation to promote cilia formation. For sptPALM imaging, samples were incubated with the addition of doxycycline (D1822; Sigma-Aldrich) to induce IFT88-mEos4b expression and then loaded into an imaging chamber (CM-B18-1; Live Cell Instrument, Nowon-gu, Seoul, Korea) filled with serum-free medium. For testing the blinking efficiency of mEos4b, cells were fixed with ice-cold methanol (32213; Sigma-Aldrich) at −20°C for 5 min before imaging.

Immunofluorescence

Cells were fixed with 4% paraformaldehyde at room temperature or methanol at −20°C for 10 min after quick rinses with phosphate-buffered saline (PBS). The cells were then permeabilized with washing solution (PBS with 0.1% Triton X-100) for 10 min and blocked with 3% bovine serum albumin for 30 min. Primary antibodies (goat IFT88 [1:100] [ab42497; Abcam, Cambridge, UK]; rabbit KIF3A [1:200] [ab11259; Abcam]; and rabbit BBS2 [1:100] [11188-2-AP; Proteintech, Rosemont, IL]) were diluted in the blocking solution. The cells were incubated in the primary antibody solution for 1 h at room temperature; this was followed by three rinses in the washing solution. The cells were then stained with secondary antibodies Alexa Fluor 647 (A21447; Thermo Fisher Scientific) and Cy3B (conjugating Cy3B maleimide; PA63131; GE, Pittsburgh, PA) to immunoglobulin G antibodies (711-005-152; Jackson, West Grove, PA)) for 1 h before being washed five times.

Single molecule–localization imaging

sptPALM and dSTORM imaging were performed on a modified inverted microscope (Nikon Eclipse Ti-E; Nikon, Tokyo, Japan). The excitation lasers (OBIS 637 LX 140 mW and OBIS 488 LX 150 mW; Coherent, Santa Clara, CA; and Jive 561 150 mW; Cobolt, Solna, Sweden) and the activation laser (OBIS 405 LX 100 mW; Coherent) were coupled into a single-mode fiber and focused on the back aperture of a high numerical aperture objective (100×/1.49 NA Apo TIRF; Nikon) for wide-field illumination. Samples were placed on a motorized three-axis stage incorporated with a Perfect Focus System (PFS; Nikon) to maintain a drift-free focus. For sptPALM imaging, the cells containing mEos4b-IFT88 were first imaged with a 488-nm laser to search for primary cilia and then illuminated with an intense (1–2 kW/cm^2) 561-nm laser. For dual-color dSTORM imaging, Alexa 647 and Cy3B were imaged sequentially with 637- and 561-nm light (2–5 kW/cm^2), respectively. A weak 405-nm light (<5 W/cm^2) was used to activate a portion of the probes converted from a dark state to an excitation state. During the acquisition, fixed samples were incubated in an imaging buffer containing Tris-sodium chloride buffer at pH 8.0 and an oxygen-scavenging system (70–80 mM mercaptoethylamine, 0.5 mg/ml glucose oxidase, 40 µg/ml catalase, and 10% [wt/vol] glucose) (Sigma-Aldrich). The fluorescence signals were cleaned by emission filters (525/50, 593/40, and 700/75 nm; Chroma, Bellows Falls, VT) and imaged using an EMCCD (Evolve 512 Delta; Photometrics, Tucson, AZ) with a pixel size of 93 nm. For sptPALM, 5000–10,000 frames were recorded at an acquisition rate of 33/s; and for dSTORM, 10,000–20,000 frames were taken at a rate of 50/s. The peaks of individual single molecules were localized using the MetaMorph superresolution module (Molecular Devices, Sunnyvale, CA). During the live-cell imaging, RPE-1 cells were maintained in DMEM/F-12 without phenol red and incubated in a chamber heated at 37°C (TC-A/CU-501; Live Cell Instrument). Each sample was imaged for no more than 1 h. To systematically minimize the influence of temperature-induced drift, we added fluorescent fiducial marker (Tetraspeck; Thermo Fisher) onto both live and fixed samples at 1/200 dilution to detect drift during acquisition for postacquisition correction with ImageJ.

Analytical methods

Single-molecule tracking. Single-molecule tracking was performed via the MetaMorph superresolution module based on wavelet segmentation (Izeddin *et al.*, 2012; Kechkar *et al.*, 2013) and simulated annealing algorithms (Racine *et al.*, 2006; Sibarita, 2014) for particle localization and tracking (running with a minimum length of 5 frames and a maximum search distance of 2 pixels from current point to next point) to obtain trajectories. The data from quasi-stationary cilia during an ~5-min acquisition were selected by evaluating their accumulative deviation from the nominal width and their localization pattern. A systematic characterization of the shifting effect under the quasi-stationary condition is shown in Supplemental Figure S1. In general, the shifting timescale is two orders of magnitude slower than that of active transport of IFT molecules.

Effective displacement and effective velocity analysis. Every trajectory was linearly fitted to determine its initial and final location and then described as the effective displacement (Supplemental Figure S5). For generating the effective displacement plot, as shown in Figure 2B or Supplemental Figure S7, data from different primary cilia were combined into the same coordinate system. To do this, a coordinate system adapted according to the orientation of a cilium was defined at its base. Each of the primary cilia was fitted with a spline curve and then straightened according to this curve in ImageJ. Images were aligned vertically and laterally with respect to the widest axial position at the DAPs and the spline curve. All trajectories containing the location information of

particles were transformed onto the new coordinate system (Supplemental Figure S6). To ensure a meaningful quantification of displacement for each trajectory, we only picked trajectories with effective displacement greater than 45 nm, that is, the system resolution. The effective velocity is calculated based on the effective displacement, defined as effective displacement over duration of the corresponding single-molecule emission.

Kymograph analysis. For kymograph analysis shown in Figure 1D and Supplemental Figure S4, single-molecule signals were extracted only along the fitted curve for a given cilium where the spline curve starts from the base of the cilium. Kymographs were then generated from video streams of 5000–10,000 frames via Multi Kymograph (ImageJ) with a line width of 3 pixels to identify single-molecule events. To create kymographs like the one in Figure 1D, a long kymograph was reshaped into several segments combined. Given the direction of a spline curve, trails of a positive slope indicate the movement from the ciliary tip to the base and vice versa. A vertical trail indicates the stationary movement along the defined curve.

Consecutive displacement analysis. For the consecutive displacement (translocation) analysis shown in Figure 3A, the displacements were calculated based on each distance between two consecutive locations of a trajectory that was generated as described earlier. Thousands of consecutive displacements from multiple cilia were transformed to the same coordinate before being combined. To create a map of consecutive displacements as shown in Figure 3A, we used the middle points of individual displacements as their presented locations and generated a scatter plot from these locations and the corresponding displacements. For the statistical analysis, we extracted the data from four different ciliary compartments based on the pattern of IFT88 (Yang *et al.*, 2015); that is, y = [–100 nm, 100 nm] for DAP; y = [100 nm, 200 nm] for pTZ; y = [200 nm, 400 nm] for dTZ; y = [400 nm, 2000 nm] for CC.

MSD and diffusive parameter α analysis. To gain insight into diffusive characteristics of molecule transport, we further computed the MSD of the IFT protein for each trajectory according to the following formula (Meijering *et al.*, 2012):

$$\mathrm{MSD}(n) = \frac{1}{N-n}\sum_{i=1}^{N-n} d^2(\mathrm{P}_i, \mathrm{P}_{i+n})$$

where N is the total number of time points of a trajectory; n is the number of time intervals; and $d(\mathrm{P}_i, \mathrm{P}_{i+n})$ is the distance between two points P_i and P_{i+n}.

MSD is a function of time lag and allows one to characterize the mode of motion. We adopted a general formula for describing the relationship between the MSD, the diffusion parameter (α), and the diffusion coefficient (D) given below for 2D particle tracking (Meijering *et al.*, 2012):

$$\mathrm{MSD}(t) = 4Dt^{\alpha}$$

where t is the time lag and the diffusion mode is dependent on α, with $\alpha < 1$ characterized as subdiffusion and $\alpha > 1$ as superdiffusion. The diffusion analysis herein enables the classification of IFT particle movement into superdiffusion, movement that behaves like directional motion driven by active transport, and subdiffusion, movement that behaves like spatially confined motion, possibly due to obstruction. Thus, we first plotted the MSD curve t for each trajectory and then fitted the curve with the above equation to calculate the α value. For the optimal estimation of diffusion mode, we calculated the optimal fitting point for each MSD curve based on an empirical approximation (Michalet, 2010). The data in Figure 3, E–G, were analyzed by screening trajectories with a length of more than 7 frames and an α value of 0–2.5 to minimize fitting errors and artifacts.

Assay for the effect of pH on single-molecule event. We examined the blinking characteristics of mEos4b in fixed samples at four different pH conditions (6, 7.2, 8, 9) in a PBS-based buffer. Each sample was imaged for 5000–10,000 frames, and then the acquired stream video was analyzed to generate a kymograph (Supplemental Figure S3A). For determining whether each blinking signal is spatially separate, a raw kymograph was first filtered to smooth the discrete signals caused by fast blinking within each trail. The image was then converted to a binary format for region size analysis and for each trail yielded a width and a length for which the width indicated the degree of signal overlap and the length was proportional to the duration of an emitter (Supplemental Figure S3D). A threshold of 6 pixels in width was chosen to differentiate between the defined single-emitter events and multi-emitter events. The ratio at different pH levels is shown in Supplemental Figure S3B. The fraction of single-emitter events of more than 10 frames is compared in Supplemental Figure S3C.

Statistical analysis

Our experimental data were analyzed based on eight biologically independent experiments. Quantified values that passed the statistical assumption test were subjected to the two-tailed Student's t test using GraphPad Prism. The n values used to derive statistical analysis are noted in the figure legends.

ACKNOWLEDGMENTS

We thank Won-Jing Wang for sharing reagents and Chia-Lung Hsieh for comments on the article. This work was supported by the Ministry of Science and Technology, Taiwan (grant no. 103-2112-M-001-039-MY3, 107-2112-M-001-037), an Academia Sinica Career Development Award (grant no. AS-CDA-104-M06), and the National Taiwan University and Academia Sinica Innovative Joint Program (grant no. NTU-AS-106R104503).

REFERENCES

Besschetnova TY, Kolpakova-Hart E, Guan Y, Zhou J, Olsen BR, Shah JV (2010). Identification of signaling pathways regulating primary cilium length and flow-mediated adaptation. Curr Biol 20, 182–187.

Chih B, Liu P, Chinn Y, Chalouni C, Komuves LG, Hass PE, Sandoval W, Peterson AS (2011). A ciliopathy complex at the transition zone protects the cilia as a privileged membrane domain. Nat Cell Biol 14, 61–72.

Craft JM, Harris JA, Hyman S, Kner P, Lechtreck KF (2015). Tubulin transport by IFT is upregulated during ciliary growth by a cilium-autonomous mechanism. J Cell Biol 208, 223–237.

Craige B, Tsao C-C, Diener DR, Hou Y, Lechtreck K-F, Rosenbaum JL, Witman GB (2010). CEP290 tethers flagellar transition zone microtubules to the membrane and regulates flagellar protein content. J Cell Biol 190, 927–940.

Deane JA, Cole DG, Seeley ES, Diener DR, Rosenbaum JL (2001). Localization of intraflagellar transport protein IFT52 identifies basal body transitional fibers as the docking site for IFT particles. Curr Biol 11, 1586–1590.

Engel BD, Ludington WB, Marshall WF (2009). Intraflagellar transport particle size scales inversely with flagellar length: revisiting the balance-point length control model. J Cell Biol 187, 81–89.

Frost NA, Shroff H, Kong H, Betzig E, Blanpied TA (2010). Single-molecule discrimination of discrete perisynaptic and distributed sites of actin filament assembly within dendritic spines. Neuron 67, 86–99.

Garcia-Gonzalo F, Corbit K, Sirerol-Piquer M, Ramaswami G, Otto E, Noriega T, Seol A, Robinson J, Bennett C, Josifova D, *et al.* (2011).

A transition zone complex regulates mammalian ciliogenesis and ciliary membrane composition. Nat Genet 43, 776–784.
Goetz SC, Anderson KV (2010). The primary cilium: a signalling centre during vertebrate development. Nat Rev Genet 11, 331–344.
Heilemann M, van de Linde S, Schüttpelz M, Kasper R, Seefeldt B, Mukherjee A, Tinnefeld P, Sauer M (2008). Subdiffraction-resolution fluorescence imaging with conventional fluorescent probes. Angew Chem Int Ed 47, 6172–6176.
Hess ST, Gould TJ, Gudheti MV, Maas SA, Mills KD, Zimmerberg J (2007). Dynamic clustered distribution of hemagglutinin resolved at 40 nm in living cell membranes discriminates between raft theories. Proc Natl Acad Sci USA 104, 17370–17375.
Hoze N, Nair D, Hosy E, Sieben C, Manley S, Herrmann A, Sibarita J-B, Choquet D, Holcman D (2012). Heterogeneity of AMPA receptor trafficking and molecular interactions revealed by superresolution analysis of live cell imaging. Proc Natl Acad Sci USA 109, 17052–17057.
Hu Q, Milenkovic L, Jin H, Scott MP, Nachury MV, Spiliotis ET, Nelson WJ (2010). A septin diffusion barrier at the base of the primary cilium maintains ciliary membrane protein distribution. Science 329, 436–439.
Ishikawa H, Marshall WF (2011). Ciliogenesis: building the cell's antenna. Nat Rev Mol Cell Biol 12, 222–234.
Izeddin I, Boulanger J, Racine V, Specht CG, Kechkar A, Nair D, Triller A, Choquet D, Dahan M, Sibarita J-B (2012). Wavelet analysis for single molecule localization microscopy. Opt Express 20, 2081–2095.
Izeddin I, Récamier V, Bosanac L, Cissé II, Boudarene L, Dugast-Darzacq C, Proux F, Bénichou O, Voituriez R, Bensaude O, *et al*. (2014). Single-molecule tracking in live cells reveals distinct target-search strategies of transcription factors in the nucleus. eLife 3, e02230.
Kechkar A, Nair D, Heilemann M, Choquet D, Sibarita J-B (2013). Real-time analysis and visualization for single-molecule based super-resolution microscopy. PLoS One 8, e62918.
Kee HL, Dishinger JF, Lynne Blasius T, Liu C-J, Margolis B, Verhey KJ (2012). A size-exclusion permeability barrier and nucleoporins characterize a ciliary pore complex that regulates transport into cilia. Nat Cell Biol 14, 431–437.
Kozminski KG, Johnson KA, Forscher P, Rosenbaum JL (1993). A motility in the eukaryotic flagellum unrelated to flagellar beating. Proc Natl Acad Sci USA 90, 5519–5523.
Manley S, Gillette J, Patterson G, Shroff H, Hess H, Betzig E, Lippincott-Schwartz J (2008). High-density mapping of single-molecule trajectories with photoactivated localization microscopy. Nat Methods 5, 155–158.
Meijering E, Dzyubachyk O, Smal I (2012). Methods for cell and particle tracking. Methods Enzymol 504, 183–200.
Michalet X (2010). Mean square displacement analysis of single-particle trajectories with localization error: Brownian motion in an isotropic medium. Phys Rev E 82, 041914.
Mijalkovic J, Prevo B, Oswald F, Mangeol P, Peterman EJG (2017). Ensemble and single-molecule dynamics of IFT dynein in *Caenorhabditis elegans* cilia. Nat Commun 8, 14591.
Milenkovic L, Weiss LE, Yoon J, Roth TL, Su YS, Sahl SJ, Scott MP, Moerner WE (2015). Single-molecule imaging of Hedgehog pathway protein Smoothened in primary cilia reveals binding events regulated by Patched1. Proc Natl Acad Sci USA 112, 8320–8325.
Nachury M, Loktev A, Zhang Q, Westlake C, Peranen J, Merdes A, Slusarski D, Scheller R, Bazan J, Sheffield V, *et al*. (2007). A core complex of BBS proteins cooperates with the GTPase Rab8 to promote ciliary membrane biogenesis. Cell 129, 1201–1213.
Nachury MV, Seeley ES, Jin H (2010). Trafficking to the ciliary membrane: how to get across the periciliary diffusion barrier? Annu Rev Cell Dev Biol 26, 59–87.
Oswald F, Prevo B, Acar S, Peterman EJG (2018). Interplay between ciliary ultrastructure and IFT-train dynamics revealed by single-molecule super-resolution imaging. Cell Rep 25, 224–235.
Ou G, Blacque OE, Snow JJ, Leroux MR, Scholey JM (2005). Functional coordination of intraflagellar transport motors. Nature 436, 583–587.
Paez-Segala MG, Sun MG, Shtengel G, Viswanathan S, Baird MA, Macklin JJ, Patel R, Allen JR, Howe ES, Piszczek G, *et al*. (2015). Fixation-resistant photoactivatable fluorescent proteins for CLEM. Nat Methods 12, 215–218.
Pedersen LB, Geimer S, Rosenbaum JL (2006). Dissecting the molecular mechanisms of intraflagellar transport in *Chlamydomonas*. Curr Biol 16, 450–459.
Persson F, Linden M, Unoson C, Elf J (2013). Extracting intracellular diffusive states and transition rates from single-molecule tracking data. Nat Methods 10, 265–269.
Prevo B, Mangeol P, Oswald F, Scholey JM, Peterman EJG (2015). Functional differentiation of cooperating kinesin-2 motors orchestrates cargo import and transport in *C. elegans* cilia. Nat Cell Biol 17, 1536–1545.
Racine V, Hertzog A, Jouanneau J, Salamero J, Kervrann C, Sibarita J-B (2006). Multiple-target tracking of 3D fluorescent objects based on simulated annealing. Third IEEE International Symposium on Biomedical Imaging: Nano to Macro, held April 6–9, 2006, in Arlington, VA, 1020–1023.
Reiter JF, Blacque OE, Leroux MR (2012). The base of the cilium: roles for transition fibres and the transition zone in ciliary formation, maintenance and compartmentalization. EMBO Rep 13, 608–618.
Rosenbaum JL, Witman GB (2002). Intraflagellar transport. Nat Rev Mol Cell Biol 3, 813–825.
Rossier O, Octeau V, Sibarita J-B, Leduc C, Tessier B, Nair D, Gatterdam V, Destaing O, Albigès-Rizo C, Tampé R, *et al*. (2012). Integrins β1 and β3 exhibit distinct dynamic nanoscale organizations inside focal adhesions. Nat Cell Biol 14, 1057–1067.
Sibarita J-B (2014). High-density single-particle tracking: quantifying molecule organization and dynamics at the nanoscale. Histochem Cell Biol 141, 587–595.
Singla V, Reiter J (2006). The primary cilium as the cell's antenna: signaling at a sensory organelle. Sci STKE 313, 629–633.
Snow JJ, Ou G, Gunnarson AL, Walker MRS, Zhou HM, Brust-Mascher I, Scholey JM (2004). Two anterograde intraflagellar transport motors cooperate to build sensory cilia on *C. elegans* neurons. Nat Cell Biol 6, 1109–1113.
Tanos BE, Yang H-J, Soni R, Wang W-J, Macaluso FP, Asara JM, Tsou M-FB (2013). Centriole distal appendages promote membrane docking, leading to cilia initiation. Genes Dev 27, 163–168.
Taschner M, Bhogaraju S, Lorentzen E (2012). Architecture and function of IFT complex proteins in ciliogenesis. Differentiation 83, S12–S22.
Tran PV, Haycraft CJ, Besschetnova TY, Turbe-Doan A, Stottmann RW, Herron BJ, Chesebro AL, Qiu H, Scherz PJ, Shah JV, *et al*. (2008). THM1 negatively modulates mouse sonic hedgehog signal transduction and affects retrograde intraflagellar transport in cilia. Nat Genet 40, 403–410.
Wei Q, Zhang Y, Li Y, Zhang Q, Ling K, Hu J (2012). The BBSome controls IFT assembly and turnaround in cilia. Nat Cell Biol 14, 950–957.
Williams CL, Li C, Kida K, Inglis PN, Mohan S, Semenec L, Bialas NJ, Stupay RM, Chen N, Blacque OE, *et al*. (2011). MKS and NPHP modules cooperate to establish basal body/transition zone membrane associations and ciliary gate function during ciliogenesis. J Cell Biol 192, 1023–1041.
Wren K, Craft J, Tritschler D, Schauer A, Patel D, Smith E, Porter M, Kner P, Lechtreck K (2013). A differential cargo-loading model of ciliary length regulation by IFT. Curr Biol 23, 2463–2471.
Yang TT, Chong WM, Wang W-J, Mazo G, Tanos B, Chen Z, Tran TMN, Chen Y-D, Weng RR, Huang C-E, *et al*. (2018). Super-resolution architecture of mammalian centriole distal appendages reveals distinct blade and matrix functional components. Nat Commun 9, 2023.
Yang TT, Hampilos PJ, Nathwani B, Miller CH, Sutaria ND, Liao J-C (2013). Superresolution STED microscopy reveals differential localization in primary cilia. Cytoskeleton 70, 54–65.
Yang TT, Su J, Wang W-J, Craige B, Witman GB, Bryan Tsou M-F, Liao J-C (2015). Superresolution pattern recognition reveals the architectural map of the ciliary transition zone. Sci Rep 5, 14096.
Ye F, Breslow DK, Koslover EF, Spakowitz AJ, Nelson WJ, Nachury MV (2013). Single molecule imaging reveals a major role for diffusion in the exploration of ciliary space by signaling receptors. eLife 2, e00654.
Ye F, Nager AR, Nachury MV (2018). BBSome trains remove activated GPCRs from cilia by enabling passage through the transition zone. J Cell Biol 217, 1847–1868.